

# Chemical complexity in star formation induced by stellar feedback: cores shock-formed by the supernova remnant W44.

G. Cosentino<sup>1\*</sup>, I. Jiménez-Serra<sup>2</sup>, F. Fontani<sup>3,4,5</sup>, P. Gorai<sup>6,7</sup>, C.-Y. Law<sup>3</sup>, J. C. Tan<sup>8,9</sup>, R. Fedriani<sup>10</sup>, A. T. Barnes<sup>11</sup>, P. Caselli<sup>4</sup>, S. Viti<sup>12</sup>, J. D. Henshaw<sup>13</sup>

<sup>1</sup> Institut de Radioastronomie Millimétrique, 300 Rue de la Piscine, 38400 Saint-Martin-d'Hères, France

<sup>2</sup> Centro de Astrobiología (CSIC/INTA), Ctra. de Torrejón a Ajalvir km 4, Madrid, Spain

<sup>3</sup> INAF Osservatorio Astronomico di Arcetri, Largo E. Fermi 5, 50125 Florence, Italy

<sup>4</sup> Max Planck Institute for Extraterrestrial Physics, Giessenbachstrasse 1, 85748 Garching bei München, Germany

<sup>5</sup> Laboratory for the study of the Universe and eXtreme phenomena (LUX), Observatoire de Paris, 5, place Jules Janssen, 92195 Meudon, France

<sup>6</sup> Rosseland Centre for Solar Physics, University of Oslo, PO Box 1029 Blindern, 0315 Oslo, Norway

<sup>7</sup> Institute of Theoretical Astrophysics, University of Oslo, PO Box 1029 Blindern, 0315 Oslo, Norway

<sup>8</sup> Department of Space, Earth and Environment, Chalmers University of Technology, SE-412 96 Gothenburg, Sweden

<sup>9</sup> Department of Astronomy, University of Virginia, 530 McCormick Road Charlottesville, 22904-4325 USA

<sup>10</sup> Instituto de Astrofísica de Andalucía, CSIC, Glorieta de la Astronomía s/n, E-18008 Granada, Spain

<sup>11</sup> European Southern Observatory (ESO), Karl-Schwarzschild-Straße 2, 85748 Garching bei München, Germany

<sup>12</sup> Leiden Observatory, Leiden University, PO Box 9513, 2300 RA Leiden, The Netherlands

<sup>13</sup> Astrophysics Research Institute, Liverpool John Moores University, 146 Brownlow Hill, Liverpool L3 5RF, UK

Received September 15, 1996; accepted March 16, 1997

## ABSTRACT

**Context.** Low-velocity shocks from Supernova Remnants (SNRs) may set the physical and chemical conditions of star formation in molecular clouds. Recent evidence suggests that even the Sun might have formed through this process. However, the chemical conditions of shock-induced star forming regions remain poorly constrained.

**Aims.** We study the chemical complexity of a shock-impacted clump, with potential to yield star formation, named the Clump, and located at the interface between the SNR W44 and the infrared dark cloud G034.77-00.55. We test whether the Clump has chemical properties consistent with those observed in star forming regions unaffected by SNRs.

**Methods.** We use high-sensitivity, broad spectral surveys at 3 and 7 mm obtained with the 30m antenna at the Instituto de Radioastronomía Millimétrica and the 40 m antenna at the Yebes observatory, to identify D-bearing molecules and complex organic molecules (COMs) toward the Clump. For all species, we estimate molecular abundances and compare them with those observed across star forming regions at different evolutionary stages and masses, as well as comets.

**Results.** We detect multiple deuterated molecules (DCO<sup>+</sup>, DNC, DCN, CH<sub>2</sub>DOH) and COMs (CH<sub>3</sub>OH, CH<sub>3</sub>CHO, CH<sub>3</sub>CCH, CH<sub>3</sub>CN, CH<sub>3</sub>SH) with excitation temperatures of 5–13 K. To the best of our knowledge, this is the first detection of COMs toward a site of SNR–cloud interaction. The derived D/H ratios (~0.01–0.04) and COM abundances are consistent with those reported toward typical low-mass starless cores and comparable to cometary values. The overall level of chemical complexity is relatively low, in line with an early evolutionary stage.

**Conclusions.** We suggest that the Clump is an early stage shock-induced low-mass star forming region, not yet protostellar. We speculate that SNR-driven shocks may set the physical and chemical conditions to form stars. The resulting chemical budget may be preserved along the formation process of a planetary system, being finally incorporated into planetesimals and comets.

**Key words.** ISM: bubbles – ISM: clouds – ISM: molecules – ISM: supernova remnants – ISM: individual objects: W44 - ISM: individual objects: G034.77-00.55

## 1. Introduction

Supernova Remnants (SNRs) are among the most energetic (Bally 2011) and long-lasting (Leitherer et al. 1999; Agertz et al. 2013) sources of feedback that affect the Interstellar Medium (ISM). Relatively slow shocks (a few tens of km s<sup>-1</sup>) driven by late stages expanding SNR shells can sweep up the surrounding material, increasing its density (Inoue et al. 2018; Cosentino et al. 2019, 2022; Sano et al. 2020, 2023) and enhancing its star formation potential (Barnes et al. 2023; Khullar et al. 2024; Beattie et al. 2025). The resulting high

post-shock densities enable rapid gas cooling and enhanced chemical reactions (Fragile et al. 2003), which can in turn trigger gravitational collapse even of initially stable clouds (Li et al. 2014). Recent simulations further suggest that shocks can funnel gas into filaments, setting the conditions under which gravity can drive star formation (Federrath & Klessen 2012; Appel et al. 2023).

There is also growing evidence that even our own Sun may have formed within a massive star-forming region shaped by stellar feedback (Adams 2010; Gounelle & Meynet 2012; Pfalzner et al. 2015), where at least one nearby supernova played a pivotal role (Boss & Keiser 2013; Young 2014; Parker et al.

\* E-mail:cosentino@iram.fr

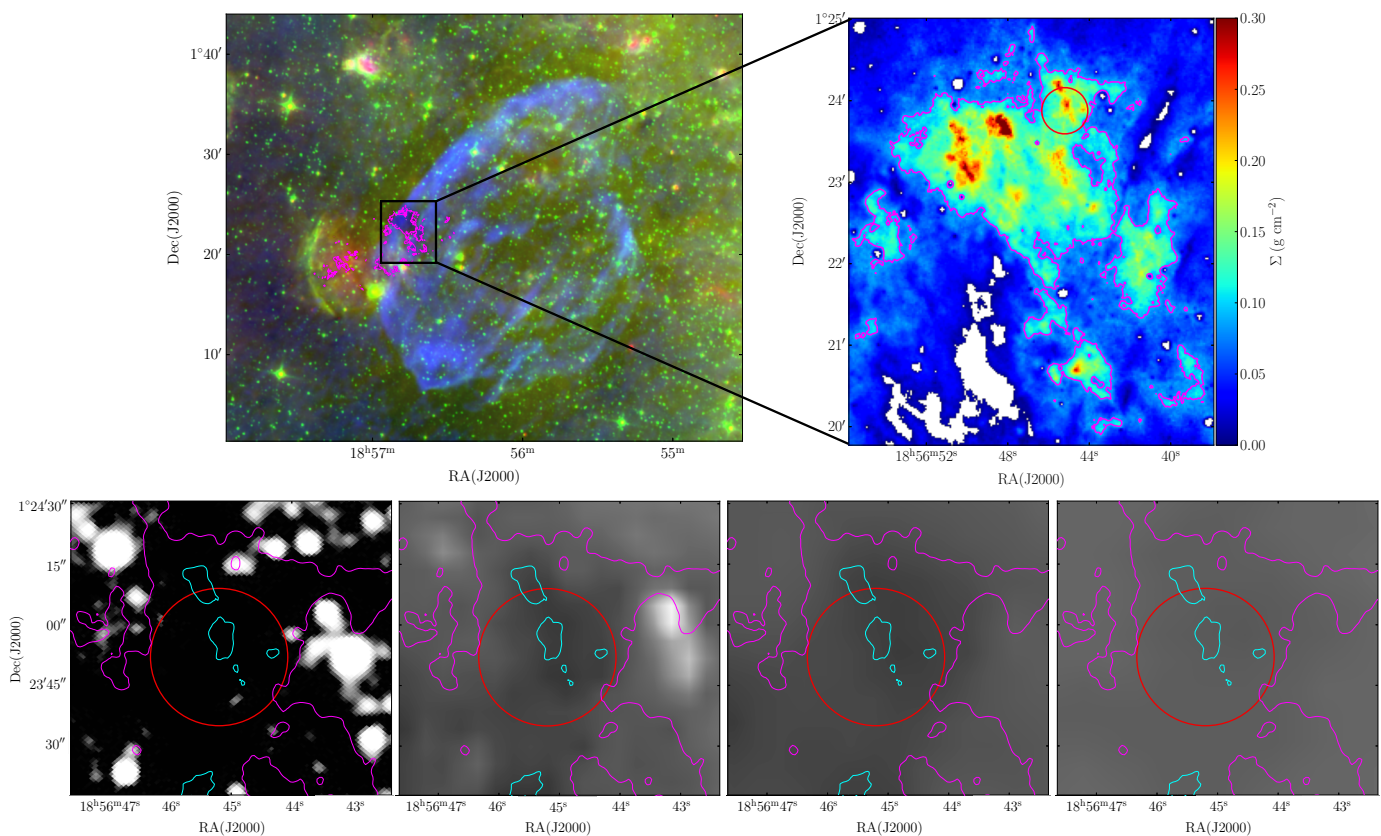


**Fig. 1.** *Top Left:* Three colour image of G34.77. Red is  $24\ \mu\text{m}$  emission from the MIPS GAL survey (Carey et al. 2009), green is  $8\ \mu\text{m}$  emission from the GLIMPSE survey (Churchwell et al. 2009) and blue is 1 GHz continuum emission from the THOR survey (Beuther et al. 2016). *Top Right:* Mass surface density map (color scale; Kainulainen & Tan 2013) with the red circle indicating the location of the Clump. *Bottom panels:* Zoom-in views of the Clump at  $2\ \mu\text{m}$  (2MASS; Skrutskie et al. 2006),  $8\ \mu\text{m}$  (Carey et al. 2009),  $24\ \mu\text{m}$  (Churchwell et al. 2009) and  $70\ \mu\text{m}$  (Hi-GAL Molinari et al. 2010) emission. The cyan contours correspond to a mass surface density value of  $0.1\ \text{g cm}^{-2}$  and highlights the cloud outskirts. The red circle size corresponds to  $44''$ , i.e. the largest beam size in the Yebes-40m observations.

2023). According to this scenario, a supernova shock impacting the proto-solar core may have triggered its collapse, while simultaneously enriching the material with radioactive and chemically processed ejecta (e.g. Boss & Keiser 2010). The presence of short-lived radionuclides, such as  $^{26}\text{Al}$  and  $^{60}\text{Fe}$ , in primitive meteorites supports this scenario (Ouellette et al. 2007, 2009; Desch et al. 2022). It has also been suggested that the Sun, as other Sun-like stars, may have emerged within complex hub-filament systems, where star formation is promoted by filament mergers induced by both early feedback in the form of HII regions and later-stage shocks from SNRs (Arzoumanian et al. 2023).

Studying chemical complexity in dense cores within molecular clouds that are affected by the interaction with SNRs offers a unique opportunity to probe this scenario. However, direct observations of these environments remain scarce. Toward the SNRs W41 (Hogge et al. 2019) and IC443 (Reach et al. 2024), indirect evidence of cores has been reported, but these may have pre-existed the shock and be negatively affected by it i.e., the shock is dispersing them, making it unlikely that they will collapse to form stars (Zhou et al. 2021; Cosentino et al. 2022; Reach et al. 2024). More recently, Cosentino et al. (2025) have identified signatures of early-stage star formation towards the Infrared Dark Cloud (IRDC) G034.77-00.55 (thereafter G034.77), shock-interacting with the nearby SNR W44. W44 is a 20k years old, core-collapse, SNR located 2.9 kpc away (Lee et al.

2020) and driving a relatively slow shock ( $\sim 15\text{-}20\ \text{km s}^{-1}$ ; Sashida et al. 2013; Cosentino et al. 2019) into the western edge of G034.77. The author used high-angular resolution  $\text{N}_2\text{H}^+$  (1-0) ALMA images to reveal the presence of multiple cores at the shock interface. Several factors support the scenario that the cores formation may have been triggered by the shock passage. The density of the post-shocked gas ( $\geq 10^6\ \text{cm}^{-3}$ ), traced by  $\text{C}^{18}\text{O}$  in Cosentino et al. (2019) and  $\text{N}_2\text{H}^+$  in Cosentino et al. (2025), has been reported to be consistent with that typically found in star forming regions (Cosentino et al. 2019). This dense post-shocked gas is significantly blue-shifted ( $39\text{-}42\ \text{km s}^{-1}$  Cosentino et al. 2019) with respect to the main cloud's velocity ( $43\text{-}45\ \text{km s}^{-1}$  Rathborne et al. 2006; Hernandez & Tan 2015). The cores identified by Cosentino et al. (2025) show densities and kinematics consistent with that of the post-shocked gas. Moreover, the cores are distributed along two filaments whose orientation is consistent with that of the shock front. In Cosentino et al. (2023), the D/H ratio toward the post-shocked material was reported to be enhanced with respect to the inner cloud and comparable to that of other early stage star forming regions. Finally, the presence of  $\text{N}_2\text{D}^+$  emission in the post-shocked gas suggests that this is likely dense and cold material, i.e. it has high potential to harbour star formation. Hence, the kinematic and morphological link between the post-shocked gas and the cores, as well as their similar physical conditions, suggests that the cores formation might have been enabled by the shock passage. The shock is therefore responsible for setting

physical conditions within the cores that are similar to those observed in star forming regions.

The majority of the cores appear gravitationally unstable considering thermal and turbulent support. In the 1.2 mm maps obtained by Rathborne et al. (2006) with the IRAM-30m MAMBO II instrument (11" or 0.15 pc) and in the 3 mm ALMA images (3" or 0.04 pc) reported by Barnes et al. (2021) and Cosentino et al. (2019) no continuum emission is found toward the cores. Finally, the cores are not associated with point-like sources at 8, 24 and/or 70  $\mu\text{m}$  (Paron et al. 2009; Barnes et al. 2016), suggesting that no central protostars are present toward the cores. In light of all this, Cosentino et al. (2025) have suggested that shocks driven by the SNR W44 may have impacted the cloud, enhanced the gas density and triggered the formation of the identified cores. Hence, the cores may be regions of shock-induced star-formation.

Across the region of G034.77 where the core population is located, the pointing previously identified as Clump (Cosentino et al. 2023) has the highest star formation potential (Cosentino et al. 2025). It shows high mass surface density  $\Sigma > 0.1 \text{ g cm}^{-2}$  and a D/H ratio of  $\sim 0.1$ , measured as the ratio between the  $\text{N}_2\text{D}^+$  and  $\text{N}_2\text{H}^+$  column densities obtained with single-pointing observations. This is consistent with values typically measured in both low-mass (Crapsi et al. 2005; Friesen et al. 2013; Cheng et al. 2021) and high-mass (Fontani et al. 2006, 2011; Kong et al. 2016) starless and pre-stellar cores. Therefore, the Clump has the potential to be a unique laboratory for investigating the chemical complexity of prestellar cores whose formation might have been induced by stellar feedback.

In this work, we investigate the Clump chemical inventory, also in relation with that of Galactic star forming regions at different evolutionary stages, as well as meteorites and comets, likely carriers of the pristine proto-solar environment. In particular, we measure deuterium fractionation in multiple species and assess the presence of complex organic molecules (COMs). D/H ratios derived from different tracers are valuable complementary indicators of a core's evolutionary stage (Fontani et al. 2006; Caselli et al. 2008; Ceccarelli et al. 2014; Bianchi et al. 2017; Sabatini et al. 2019; Bovino et al. 2021; Colzi et al. 2022). For instance, deuterium fractionation measured from  $\text{N}_2\text{D}^+$  and  $\text{N}_2\text{H}^+$  increases during the starless/prestellar phase and decreases during the proto-stellar phase (Crapsi et al. 2005; Emprechtinger et al. 2009). On the other hand, deuteration measured from HNC and  $\text{HCO}^+$  have less steep decline (Fontani et al. 2014; Gerner et al. 2015). For instance, Fontani et al. (2015) found that the DNC/HNC column density ratio is less sensitive than the  $\text{N}_2\text{D}^+/\text{N}_2\text{H}^+$  ratio across different stages of high-mass star formation.

COMs have been detected in a wide variety of environments (see Ceccarelli et al. 2022, for a review). Traditionally associated with hot cores (e.g. Brown et al. 1975; Blake et al. 1987) and corinos (Cazaux et al. 2003; Bianchi et al. 2019; Martín-Doménech et al. 2021), COMs have also been observed in starless and pre-stellar cores (e.g. Jiménez-Serra et al. 2016; Scibelli et al. 2021; Megías et al. 2023; Scibelli et al. 2024), dark clouds (e.g. Agúndez et al. 2015; Marcelino et al. 2020; Cernicharo et al. 2021), translucent clouds (Thiel et al. 2017), and protoplanetary disks (e.g. Walsh et al. 2014). Their abundance evolution during the star-formation process has been investigated in recent studies (Coletta et al. 2020; Bhat et al. 2023), which indicates an increasing trend from the starless/pre-stellar phase to the protostellar phase.

The paper is organised as follows. In Sect. 2, we describe data and observation strategy. In Sect. 3, we identify the molecular species of interest and measure their abundances. In Sect. 4, we present and discuss our results. Finally, in Sect. 5, we present our conclusions.

## 2. Observations and Data

### 2.1. IRAM-30m observations

In this work, we use 3 mm and 7 mm single pointing observations obtained in March 2020 with the 30m antenna at the Instituto de Radioastronomía Millimétrica (IRAM; Pico Veleta, Spain) and in April 2024 with the 40m antenna at the Yebes Observatory (Castilla-La Mancha, Spain), respectively. Observations have been acquired toward the position previously identified as Clump by Cosentino et al. (2023) and centered at RA(J2000)= $18^{\text{h}}56^{\text{m}}45.2^{\text{s}}$ , Dec(J2000)= $1^{\text{d}}23^{\text{m}}52^{\text{s}}$ ) with off position RA(J2000)= $18^{\text{h}}57^{\text{m}}01^{\text{s}}$ , Dec(J2000)= $1^{\text{d}}22^{\text{m}}25^{\text{s}}$ . In Figure 1, the location of the IRDC G034.77 with respect to the SNR W44 is shown (top left panel). The location of the Clump within the cloud is also indicated (top right panel), as well as a zoom-in view at multiple wavelengths from archival data (bottom panels). From Figure 1, no IR signatures of deeply embedded protostars are found, confirming the results already presented by Barnes et al. (2021); Cosentino et al. (2025).

Both sets of observations were performed in dual polarisation and position-switching mode. For the IRAM-30m observations, we used the EMIR90 receiver, tuned at frequencies of 74.0 and 86.0 GHz, to cover a continuous frequency range of 71.9-102.3 GHz. We also used the FTS spectrometer with a frequency resolution of 200 kHz, corresponding to a velocity resolution between 0.7 and 0.8  $\text{km s}^{-1}$ . Intensities were measured in units of antenna temperature,  $T_A^*$ , and converted into main-beam brightness temperature,  $T_{\text{mb}}$ , using beam and forward efficiencies of 0.81 and 0.95, respectively. The angular resolution of the 30m antenna is between 34" and 24" in the 3 mm band. These correspond to a linear spatial resolution of 0.4-0.5 parsec at the distance of G34.77 i.e., 2.9 kpc (Lee et al. 2020).

### 2.2. YEBES-30m observations

The Yebes-40m observations at 7 mm were performed in Q-band, covering a continuous frequency range 31.3-49.5 GHz and using the FFT spectrometer with spectral resolution of 38 kHz ( $\sim 0.25 \text{ km s}^{-1}$ ). In order to increase the signal-to-noise ratio, we smoothed the spectra in velocity, using the function `SMOOTH` in `GILDAS` and obtaining final velocity resolution in the range 0.5-0.7  $\text{km s}^{-1}$ . Intensities were converted from  $T_A^*$  to  $T_{\text{mb}}$ , using beam and forward efficiencies of 0.61 and 0.95, respectively. Observations performed with the 40m antenna have angular resolution between 36" and 44" i.e., 0.5-0.6 pc at the source distance. All these information are summarised in Table 1. The final spectra were produced using the `CLASS` software within the `GILDAS` package<sup>1</sup> and have rms per channel between 7 and 5 mK for the IRAM-30m observations and 3-5 mK for the Yebes-40m observations.

### 2.3. MIREX map

For our analysis, we also employ the mass surface density,  $\Sigma$ , map obtained toward G034.77 by Kainulainen & Tan (2013) and

<sup>1</sup> See <http://www.iram.fr/IRAMFR/GILDAS>.

**Table 1.** Telescope, frequency ranges, rms noise ( $T_{\text{mb}}$ ), velocity resolution and beam-aperture of the observations presented in this work.

Telescope	Frequency (GHz)	rms (K)	$\delta v$ (km s <sup>-1</sup> )	Beam ( $''$ )
Yebes-40m	31.10 - 49.50	3 - 7	0.7 - 0.5	44-36
IRAM-30m	71.70 - 87.10	7 - 5	1.0 - 1.4	34-28
IRAM-30m	87.38 - 102.6	6 - 6	1.3 - 1.1	28-24

shown in the top right panel of Figure 1. In order to obtain this map, the authors extended the MIREX method previously developed by Butler & Tan (2012), combining multi-wavelengths Mid- and Near-Infrared Spitzer images of the cloud. The obtained mass surface density map has angular resolution of  $2''$ , consistent with the resolution of the Spitzer-IRAC maps and the uncertainty is estimated to be  $\sim 30\%$  (Kainulainen & Tan 2013). Since the MIREX method is not suitable to estimate mass surface densities toward sources that are bright at Mid-IR wavelengths, pixels toward which the method is not applicable appear as blank (white) in the map. For a more detailed description of the MIREX method we refer to Butler & Tan (2009, 2012) and Kainulainen & Tan (2013).

### 3. Method

#### 3.1. Line identification

The first step in our analysis is to identify species of interest in the large bandwidth spectra. For this, we have used the tool *Spectral Line Identification and Modelling*, SLIM within the MADCUBA software<sup>2</sup> (Martín et al. 2019). MADCUBA is a stand-alone, interactive tool specifically tailored for the analysis of spectra and spectral cubes. It allows to perform line identification and line modelling in Local-Thermodynamic-Equilibrium (LTE) conditions. Using the spectroscopic parameters available in the Cologne Database for Molecular Spectroscopy<sup>3</sup> (CDMS; Endres et al. 2016) and the Jet Propulsion Laboratory<sup>4</sup> (JPL; Pickett et al. 1998), we have used SLIM to identify D-bearing species (and their H-bearing counterparts) and COMs within our spectra. We consider as detection all those transitions for which the integrated intensity is at least a factor of 3 larger than the integrated noise<sup>5</sup>. In Table 2, we report the transitions, frequencies and spectral parameters as well as the integrated signal-to-noise ratio for each detected species. Among the identified deuterated species we report DCO<sup>+</sup>, DNC and DCN. Within the COMs group, we identify CH<sub>3</sub>OH, CH<sub>3</sub>CHO, CH<sub>3</sub>CCH, CH<sub>3</sub>SH and CH<sub>3</sub>CN. Moreover, we report detection of two transitions of singly-deuterated Methanol, CH<sub>2</sub>DOH. We note that bright species such as HCO<sup>+</sup>, HNC, HCN and CH<sub>3</sub>OH, counterparts to the identified D-bearing species, are detected but they are very bright and strongly suffer from optical depth effects. Hence, for further analysis, we consider their <sup>13</sup>C-bearing counterparts, which are most optically thin but still significantly bright (S/N $\geq$ 50). This is confirmed by MADCUBA, which in-

<sup>2</sup> Madrid Data Cube Analysis on ImageJ is a software developed at the Center of Astrobiology (CAB) in Madrid; <http://cab.intacsic.es/madcuba/Portada.html>

<sup>3</sup> <https://cdms.astro.uni-koeln.de/>

<sup>4</sup> <https://spec.jpl.nasa.gov/>

<sup>5</sup> We consider a linewidth of 3 km s<sup>-1</sup>, typical of the detected species, and estimate the integrated noise as  $A_{\text{rms}} = \text{rms} \times \delta v \times \sqrt{N_{\text{ch}}}$ , where rms is the spectral noise,  $\delta v$  is the velocity resolution and  $N_{\text{ch}} \sim 4-6$  is the number of channel within the 3 km s<sup>-1</sup> linewidth.

dicated for all identified species optical depth  $\tau \leq 0.03$ . Within MADCUBA, we also use the function AUTOFIT to obtain the best fit to the species spectral profiles. For each species, the function assumes all transitions to have the same central velocity and linewidth and return the LTE model that best reproduces the line profile of all transitions simultaneously. The obtained best fit values of central velocity, linewidth and integrated flux are listed in Table 2.

#### 3.2. Molecular abundances

For each detected molecule, we estimate the molecular abundance with respect to H<sub>2</sub> as:

$$\chi(X) = \frac{N(X)}{N(\text{H}_2)} \quad (1)$$

where  $N(X)$  and  $N(\text{H}_2)$  are the species and the molecular Hydrogen total column densities, respectively. In order to estimate  $N(\text{H}_2)$ , we consider the mean  $\Sigma$  value within the largest beam in our observations, and convert this to total column density, using a molecular Hydrogen mass of  $m(\text{H}_2) = 3.67 \times 10^{-24}$  g, as follows:

$$N(\text{H}_2) = \frac{\Sigma}{m(\text{H}_2)} \quad (2)$$

The employed molecular Hydrogen mass also include a 10% contribution of Helium per Hydrogen atom. The derived molecular Hydrogen column density is  $N(\text{H}_2) = (3.8 \pm 1.1) \times 10^{22}$  cm<sup>-2</sup>, where the uncertainty is due to the 30% uncertainty in the  $\Sigma$  value (Kainulainen & Tan 2013).

In order to estimate the total column density,  $N(X)$ , of all the detected molecules, we first analyse species for which more than three transitions (with significantly different excitation energies) have been detected. This is the case of <sup>13</sup>CH<sub>3</sub>OH, CH<sub>3</sub>CHO, CH<sub>3</sub>CCH and CH<sub>3</sub>CN. For these species, we have used MADCUBA to build rotational diagrams from the line integrated intensities and estimate the molecule excitation temperature,  $T_{\text{ex}}$ , and total column density,  $N(X)$ . The obtained rotational diagrams are shown in Figure 2. We obtain excitation temperatures in the range  $T_{\text{ex}} \sim 5-13$  K and total column densities  $N_{\text{tot}} \sim 0.8-20 \times 10^{12}$  cm<sup>-2</sup>. We note that the  $T_{\text{ex}}$  obtained for <sup>13</sup>CH<sub>3</sub>OH and other COMs is consistent, within the uncertainty, with  $T_{\text{ex}} = 9$  K estimated for CH<sub>3</sub>OH in Cosentino et al. (2018), with the only exception is CH<sub>3</sub>CHO, for which we report a lower  $T_{\text{ex}} \sim 5$  K, in both the A and E forms.

For the remaining species listed in Table 2, we either detect only one rotational transition (H<sup>13</sup>CO<sup>+</sup>, DCO<sup>+</sup>, HN<sup>13</sup>C, DNC) or multiple transitions with very little energy difference, i.e. not sufficient to build rotational digrams (H<sup>13</sup>CN, DCN and CH<sub>2</sub>DOH). For these species, we fix the excitation temperature at both  $T_{\text{ex}} = 5$  K and 13 K, i.e., the minimum and maximum  $T_{\text{ex}}$  found with the multi-transition approach, and use the AUTOFIT function in SLIM to estimate the total column density. Hence, we consider the best values as the mean between the two obtained column densities and associate an uncertainty as half the difference between the two values. The obtained values are then converted into abundances using Eq. 1. Finally, for all the detected D-bearing species, we calculate the Deuterium fractionation (D/H ratio) as the ratio between the column densities of the deuterated species and its non deuterated counterpart.

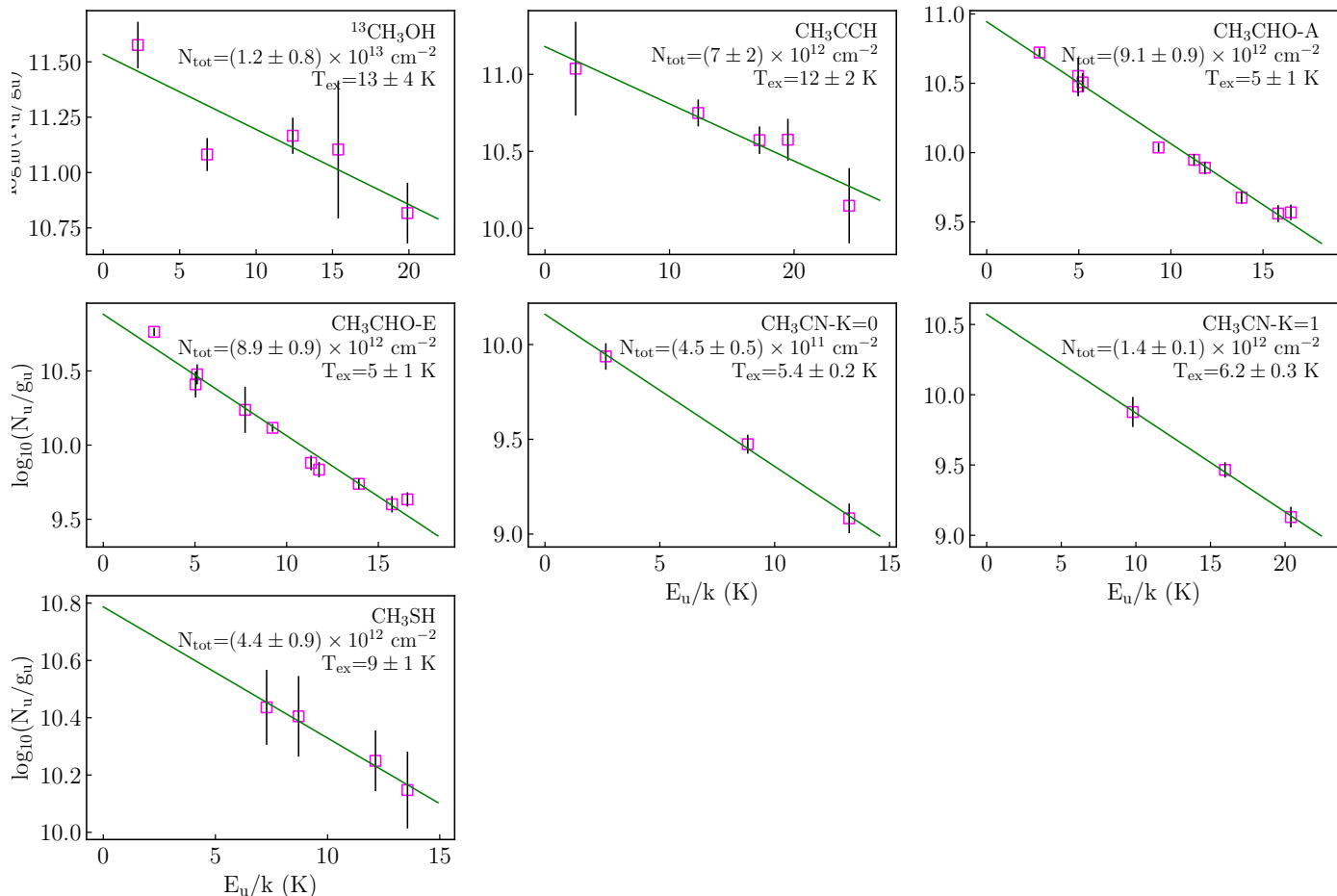


**Fig. 2.** Rotational diagrams obtained using MADCUBA for  $^{13}\text{CH}_3\text{OH}$ ,  $\text{CH}_3\text{CCH}$ ,  $\text{CH}_3\text{CHO}$ ,  $\text{CH}_3\text{CN}$  and  $\text{CH}_3\text{SH}$ . Magenta empty squares indicate the data points, while the green lines show the best fitting found by MADCUBA. In all panels, the corresponding species is indicated together with the inferred excitation temperature,  $T_{\text{ex}}$  and total column density,  $N_{\text{tot}}$ .

For the latter, when derived from the  $^{13}\text{C}$ -bearing isotopologue, we assume isotopic ratio  $^{12}\text{C}/^{13}\text{C}=49.8$ , as specifically calculated by Zeng et al. (2017) for G034.77. We also note that, as described by Parise et al. (2004) and Manigand et al. (2019), the D/H ratio from  $\text{CH}_2\text{DOH}$  and  $\text{CH}_3\text{OH}$  corresponds to 3 times the column density ratio between these species. The final value of column density, excitation temperature, molecular abundance and deuterium fractionation obtained with the above method are reported in Table 3, where we also list the COMs abundance relative to  $\text{CH}_3\text{OH}$ . The  $\text{CH}_3\text{OH}$  column density has been obtained from  $N(^{13}\text{CH}_3\text{OH})$ , assuming  $^{12}\text{C}/^{13}\text{C}=49.8$  (Zeng et al. 2017). We estimate  $N(\text{CH}_3\text{OH})=(6\pm 4)\times 10^{14} \text{ cm}^{-2}$ , a value consistent with those previously reported toward the massive cores G1, G2 and G3 within G034.77 (Cosentino et al. 2018).

We note that a filling factor = 1 was assumed in the analysis described above. This assumption was adopted because we do not know the actual source size, required to correct for the beam dilution effect. Moreover, the Clump most likely host multiple condensations (Cosentino et al. 2025) and one should also account for the number of sources within the beam. Hence, since both pieces of information are uncertain, we do not correct for

them and the COM abundance values reported here may be regarded as lower limits.

## 4. Results and Discussion

### 4.1. D-bearing Species

Using the method described in Section 3, we derive D/H ratios ranging from 0.01 to 0.09, all enhanced by several orders of magnitude with respect to the typical cosmic D/H ratio  $\sim 10^{-5}$  (Oliveira et al. 2003). The deuterium fractionation values derived from  $\text{DCO}^+$  and  $\text{DNC}$  are consistent within the uncertainties, while the D/H ratio from  $\text{DCN}$  is nearly a factor of three lower. This agrees with previous studies suggesting that D/H ratios inferred from  $\text{DCN}$  may be anti-correlated with other deuterated species i.e., it tends to be higher in more evolved sources, whereas the D/H ratio from other molecules is expected to peak at earlier phases (Fontani et al. 2015). The D/H values reported here are approximately a factor of 2–3 lower than that derived from  $\text{N}_2\text{D}^+$  ( $\sim 0.1$  Cosentino et al. 2025). This likely reflects the fact that, contrary to  $\text{N}_2\text{D}^+$ , other species may involve more complex formation pathways or be more sensitive to grain-surface chemistry (Ceccarelli et al. 2014).

In Figure 3, we compare our measurements with literature

**Table 2.** Molecular species, transition, frequency,  $A_{ul}$ ,  $E_{low}$ , integrated intensity, central velocity, linewidth and signal-to-noise ratio of all the detected transition of interest.

Molecule	Transition	Frequency (MHz)	$\log_{10}(A_{ul})$ ( $s^{-1}$ )	$E_{low}$ (K)	Area (K km s $^{-1}$ )	$v_0$ (km s $^{-1}$ )	$\Delta v$ (km s $^{-1}$ )	S/N
	$J_{k_a, k_c} - J'_{k'_a, k'_c}$							
H $^{13}$ CO $^+$	1-0	86754.288	-2.2835	0.00	1.232 $\pm$ 0.007	41.9 $\pm$ 0.1	3.2 $\pm$ 0.1	246
DCO $^+$	1-0	72039.241	-3.4952	0.00	0.177 $\pm$ 0.009	41.9 $\pm$ 0.1	3.3 $\pm$ 0.1	198
HN $^{13}$ C	1-0	87090.850	-2.5950	0.00	0.456 $\pm$ 0.04	41.8 $\pm$ 0.1	2.4 $\pm$ 0.3	17
DNC	1-0	76305.727	-2.661	0.00	0.641 $\pm$ 0.005	41.9 $\pm$ 0.1	3.3 $\pm$ 0.1	100
H $^{13}$ CN	1-0 F=1-1	86338.767	-2.9964	0.00	0.201 $\pm$ 0.003	41.9 $\pm$ 0.1	3.6 $\pm$ 0.1	30
	1-0 F=2-1	86340.184	-2.7746	0.00	0.335 $\pm$ 0.003	41.9 $\pm$ 0.1	3.6 $\pm$ 0.1	50
	1-0 F=0-1	86342.274	-3.4735	0.00	0.067 $\pm$ 0.003	41.9 $\pm$ 0.1	3.6 $\pm$ 0.1	10
DCN	1-0 F=1-1	72413.484	-3.2249	0.00	0.088 $\pm$ 0.005	41.7 $\pm$ 0.1	3.3 $\pm$ 0.3	10
	1-0 F=2-1	72414.905	-3.0031	0.00	0.147 $\pm$ 0.005	41.7 $\pm$ 0.1	3.3 $\pm$ 0.3	18
	1-0 F=0-1	72417.030	-3.7020	0.00	0.030 $\pm$ 0.005	41.7 $\pm$ 0.1	3.3 $\pm$ 0.3	5
$^{13}$ CH $_3$ OH	1 $_{0,1}$ -0 $_{0,0}$	47205.210	-5.9005	0.00	0.80 $\pm$ 0.01	41.5 $\pm$ 0.3	3.7 $\pm$ 0.6	133
	2 $_{-1,2}$ -1 $_{-1,1}$	94405.163	-5.1352	5.47	0.71 $\pm$ 0.01	41.5 $\pm$ 0.3	3.7 $\pm$ 0.6	156
	2 $_{0,2}$ -1 $_{0,1}$	94407.129	-5.0024	1.57	0.85 $\pm$ 0.01	41.5 $\pm$ 0.3	3.7 $\pm$ 0.6	189
	2 $_{1,2}$ -1 $_{1,1}$	94411.016	-5.0215	10.69	0.38 $\pm$ 0.01	41.5 $\pm$ 0.3	3.7 $\pm$ 0.6	83
CH $_2$ DOH	1 $_{0,1}$ -0 $_{0,0}$	44713.190	-6.2750	0.00	0.060 $\pm$ 0.004	41.0 $\pm$ 0.1	3.9 $\pm$ 0.3	13
	2 $_{0,2}$ -1 $_{0,1}$	89407.817	-5.3767	1.49	0.160 $\pm$ 0.004	41.0 $\pm$ 0.1	3.9 $\pm$ 0.3	21
CH $_3$ CHO	2 $_{1,2}$ -1 $_{1,1}$ (A)	37464.204	-5.6959	2.20	0.72 $\pm$ 0.005	42.0 $\pm$ 0.1	3.6 $\pm$ 0.1	193
	2 $_{1,2}$ -1 $_{1,1}$ (E)	37686.932	-5.7200	2.24	0.08 $\pm$ 0.005	42.0 $\pm$ 0.1	3.6 $\pm$ 0.1	20
	2 $_{0,2}$ -1 $_{0,1}$ (A)	38506.035	-5.5438	0.151	0.18 $\pm$ 0.005	42.0 $\pm$ 0.1	3.6 $\pm$ 0.1	45
	2 $_{0,2}$ -1 $_{0,1}$ (E)	38512.079	-5.5438	0.154	0.22 $\pm$ 0.005	42.0 $\pm$ 0.1	3.6 $\pm$ 0.1	59
	2 $_{1,1}$ -1 $_{1,0}$ (A)	39362.537	-5.6825	2.30	0.09 $\pm$ 0.005	42.0 $\pm$ 0.1	3.6 $\pm$ 0.1	22
	2 $_{1,1}$ -1 $_{1,0}$ (E)	39594.289	-5.648	2.24	0.10 $\pm$ 0.005	42.0 $\pm$ 0.1	3.6 $\pm$ 0.1	25
	4 $_{1,4}$ -3 $_{1,3}$ (A)	74891.677	-4.7041	5.33	0.17 $\pm$ 0.005	42.0 $\pm$ 0.1	3.6 $\pm$ 0.1	18
	4 $_{1,4}$ -3 $_{1,3}$ (E)	74924.134	-4.7046	5.38	0.09 $\pm$ 0.005	42.0 $\pm$ 0.1	3.6 $\pm$ 0.1	7
	4 $_{0,4}$ -3 $_{0,3}$ (A)	76866.436	-4.6506	3.92	0.18 $\pm$ 0.005	42.0 $\pm$ 0.1	3.6 $\pm$ 0.1	16
	4 $_{0,4}$ -3 $_{0,3}$ (E)	76878.953	-4.6506	3.85	0.23 $\pm$ 0.005	42.0 $\pm$ 0.1	3.6 $\pm$ 0.1	28
	4 $_{1,3}$ -3 $_{1,2}$ (A)	79099.313	-4.6581	5.59	0.13 $\pm$ 0.005	42.0 $\pm$ 0.1	3.6 $\pm$ 0.1	21
	4 $_{1,3}$ -3 $_{1,2}$ (E)	79150.166	-4.6567	5.54	0.12 $\pm$ 0.005	42.0 $\pm$ 0.1	3.6 $\pm$ 0.1	17
	2 $_{1,2}$ -1 $_{0,1}$ (A)	84219.749	-5.7339	0.64	0.05 $\pm$ 0.005	42.0 $\pm$ 0.1	3.6 $\pm$ 0.1	8
	5 $_{1,5}$ -4 $_{1,4}$ (E)	93580.909	-4.4093	7.82	0.09 $\pm$ 0.005	42.0 $\pm$ 0.1	3.6 $\pm$ 0.1	9
	5 $_{1,5}$ -4 $_{1,4}$ (A)	93595.25	-4.4093	7.87	0.07 $\pm$ 0.005	42.0 $\pm$ 0.1	3.6 $\pm$ 0.1	6
	5 $_{0,5}$ -4 $_{0,4}$ (E)	95947.437	-4.3672	6.48	0.14 $\pm$ 0.005	42.0 $\pm$ 0.1	3.6 $\pm$ 0.1	13
	5 $_{0,5}$ -4 $_{0,4}$ (A)	95963.459	-4.3672	6.42	0.12 $\pm$ 0.005	42.0 $\pm$ 0.1	3.6 $\pm$ 0.1	11
	5 $_{1,4}$ -4 $_{1,3}$ (E)	98863.314	-4.3627	8.23	0.11 $\pm$ 0.005	42.0 $\pm$ 0.1	3.6 $\pm$ 0.1	10
	5 $_{1,4}$ -4 $_{1,3}$ (A)	98900.945	-4.3622	8.18	0.10 $\pm$ 0.005	42.0 $\pm$ 0.1	3.6 $\pm$ 0.1	9
	3 $_{1,3}$ -2 $_{0,2}$ (E)	101343.441	-5.4569	1.99	0.04 $\pm$ 0.005	42.0 $\pm$ 0.1	3.6 $\pm$ 0.1	4
CH $_3$ CCH	2 $_1$ -1 $_1$	34182.755	-5.9303	5.58	0.040 $\pm$ 0.005	41.5 $\pm$ 0.06	2.9 $\pm$ 0.3	5
	2 $_0$ -1 $_0$	34183.420	-5.7949	0.57	0.020 $\pm$ 0.005	41.5 $\pm$ 0.06	2.9 $\pm$ 0.3	5
	5 $_1$ -4 $_1$	85455.622	-4.6417	10.70	0.050 $\pm$ 0.005	41.5 $\pm$ 0.06	2.9 $\pm$ 0.3	5
	5 $_0$ -4 $_0$	85457.272	-4.6135	5.70	0.090 $\pm$ 0.005	41.5 $\pm$ 0.06	2.9 $\pm$ 0.3	9
	6 $_1$ -5 $_1$	102546.024	-4.4052	13.55	0.04 $\pm$ 0.005	41.5 $\pm$ 0.06	2.9 $\pm$ 0.3	3
	6 $_0$ -5 $_0$	102547.984	-4.3825	8.55	0.08 $\pm$ 0.005	41.5 $\pm$ 0.06	2.9 $\pm$ 0.3	7
CH $_3$ SH	3 $_{0,3}$ -2 $_{0,2}$ (A $^+$ )	75862.889	-5.0852	2.53	0.050 $\pm$ 0.005	41.8 $\pm$ 0.1	2.8 $\pm$ 0.3	5
	3 $_{0,3}$ -2 $_{0,2}$ (E $^+$ )	75864.422	-5.0869	3.52	0.040 $\pm$ 0.005	41.8 $\pm$ 0.1	2.8 $\pm$ 0.3	4
	4 $_{0,4}$ -3 $_{0,3}$ (A $^+$ )	101139.150	-4.7166	5.06	0.050 $\pm$ 0.005	41.8 $\pm$ 0.1	2.8 $\pm$ 0.3	9
	4 $_{0,4}$ -3 $_{0,3}$ (E $^+$ )	101139.654	-4.7183	6.05	0.050 $\pm$ 0.005	41.8 $\pm$ 0.1	2.8 $\pm$ 0.3	9
CH $_3$ CN	2 $_1$ -1 $_1$ F=1-1	36794.765	-4.5607	5.58	0.020 $\pm$ 0.005	41.4 $\pm$ 0.1	2.8 $\pm$ 0.3	5
	2 $_0$ -1 $_0$ F=2-1	36795.475	-4.4253	0.61	0.03 $\pm$ 0.005	41.4 $\pm$ 0.1	2.8 $\pm$ 0.3	5
	4 $_1$ -3 $_1$ F=4-4	73588.799	-3.5684	8.65	0.082 $\pm$ 0.005	41.4 $\pm$ 0.1	2.8 $\pm$ 0.3	7
	4 $_0$ -3 $_0$ F=3-2	73590.218	-3.5299	3.68	0.104 $\pm$ 0.005	41.4 $\pm$ 0.1	2.8 $\pm$ 0.3	8
	5 $_1$ -4 $_1$ F=6-5	91985.314	-3.2731	11.10	0.118 $\pm$ 0.005	41.4 $\pm$ 0.1	2.8 $\pm$ 0.3	9
	5 $_0$ -4 $_0$ F=5-4	91987.088	-3.2450	6.14	0.147 $\pm$ 0.005	41.4 $\pm$ 0.1	2.8 $\pm$ 0.3	10

values for low-mass starless/pre-stellar cores (Hirota et al. 2001; Redaelli et al. 2019; van Gelder et al. 2021; Petrashkevich et al. 2024; Ambrose et al. 2024) and low-mass protostars (Hirota et al. 2001; Jørgensen et al. 2004; Emprechtinger et al. 2009; Imai et al. 2018; van Gelder et al. 2021), high-mass

IR-dark clump (Gerner et al. 2015; Kai et al. 2024), high-mass protostellar objects (Gerner et al. 2015; van Gelder et al. 2022; Boucasse et al. 2022) and comets (Meier et al. 1998; Biver et al. 2019; Despois et al. 2005; Crovisier et al. 2004; Drozdovskaya et al. 2021). We find that the D/H ratios derived

**Table 3.** Molecular species, total column density, excitation temperature, molecular abundance with respect to H<sub>2</sub>, Deuterium fractionation values and COM abundances with respect to CH<sub>3</sub>OH obtained for all the species of interest.

Molecule	$N_{\text{tot}}$ ( $\times 10^{12} \text{ cm}^{-2}$ )	$T_{\text{ex}}$ (K)	$\chi$ ( $\times 10^{-10}$ )	D/H	$N(\text{X})/N(\text{CH}_3\text{OH})$
H <sup>13</sup> CO <sup>+</sup>	1.61±0.02	5-13	0.4 ± 0.1	...	...
DCO <sup>+</sup>	2.78±0.04	5-13	0.7 ± 0.2	0.04±0.01	...
HN <sup>13</sup> C	1.1±0.1	5-13	0.3 ± 0.1	...	...
DNC	1.45±0.03	5-13	0.40 ± 0.03	0.03±0.01	...
H <sup>13</sup> CN	1.3±0.02	5-13	0.3 ± 0.1	...	...
DCN	0.76±0.05	5-13	0.20 ± 0.06	0.012±0.006	...
<sup>13</sup> CH <sub>3</sub> OH	12±8	13±4	3±2	...	...
CH <sub>2</sub> DOH	19±1	5-13	4.5 ± 1.6	0.09±0.06	...
CH <sub>3</sub> CCH	7±2	12±2	1.7±0.7	...	0.012±0.008
CH <sub>3</sub> CHO <sup>a</sup>	18±2	5±1	2.1±0.6	...	0.03±0.02
CH <sub>3</sub> CN	1.9±0.1	5.4-6.2	0.5±0.1	...	0.003±0.002
CH <sub>3</sub> SH	4.4±0.9	9±1	1.1±0.4	...	0.007±0.005

**Notes.** <sup>a</sup> The reported CH<sub>3</sub>CHO column density has been obtained as the sum of the A+E values.

from DCO<sup>+</sup>, DNC, and CH<sub>2</sub>DOH broadly agree with those reported for low-mass starless/prestellar cores and protostars. However, the lack of compact continuum sources at 1 and 3 mm (Rathborne et al. 2006; Barnes et al. 2021) as well as the lack of point-like IR emission (Paron et al. 2009; Barnes et al. 2021) seems to indicate that the Clump is at an early evolutionary stage, that is either pre-stellar or very early protostellar stage. On the other hand, the D/H ratio derived from DCN in the literature shows little variation across different environments. DCN lines have relatively lower S/N compared with other D-bearing tracers. Hence, the D/H measurements from DCN are usually less constrained. It is therefore more challenging to establish significant variations even considering the large samples extracted from the literature. In Figure 3, we also compare our results with typical D/H ratios reported for well-known comets (Meier et al. 1998; Biver et al. 2019; Despois et al. 2005; Crovisier et al. 2004; Drozdovskaya et al. 2021), meteorites (Busemann et al. 2006; Remusat et al. 2006; Robert 2003; Alexander et al. 2007, 2010, 2012, 2017), and the protosolar nebula (Lellouch et al. 2001). The latter value is derived from measurements of Jupiter. Our values are consistent within the uncertainties with those reported for comets, although these are often upper limits. On the other hand, our values are systematically higher by at least one order of magnitude than the protosolar nebula and meteorites values. We speculate that this discrepancy may be due to the fact that multiple chemical resets may occur between the shock-induced star formation and the final planetary system stage (Romero-Mirza et al. 2022; Öberg et al. 2023). In light of all this, the Clump is most likely consistent with a pre-stellar core-like deuterium chemistry.

#### 4.2. Complex Organic Molecules

Within our high-sensitivity, broad bandwidth spectra, we have detected several complex molecules, i.e., <sup>13</sup>CH<sub>3</sub>OH, CH<sub>3</sub>CCH, CH<sub>3</sub>CHO, CH<sub>3</sub>CN and CH<sub>3</sub>SH. This is a relatively low level of complexity compared with other typical low-mass starless and pre-stellar cores (Jiménez-Serra et al. 2016; Bianchi et al. 2017; Gorai et al. 2024). This reduced complexity may be due to G034.77 and the Clump being located further away (several kpc) than typical low-mass sources (few hundreds of pc) and/or to the poorer sensitivity of our observations. Alternatively, the lower

degree of chemical complexity may be indicative of the Clump being at an earlier evolutionary stage, similarly to what was reported by Megías et al. (2023) for other low-mass starless cores. Alternatively, beam dilution effects may prevent us from detecting more complex, fainter species. Future high-angular resolution images will allow more precise estimates and to discern between these possibilities.

Although detections of COMs in the ISM are common, information from literature is more sparse than what was presented in Section 4.1 for D-bearing molecules, and a similar comparison cannot be carried out. Therefore, we have considered, for each broad evolutionary stage and mass regime, sources that are often regarded as an archetype of that specific environment and compared COMs abundances with those estimated toward the Clump. We have considered L1544 (Vastel et al. 2014; Bizzocchi et al. 2014; Jiménez-Serra et al. 2016; Vastel et al. 2019; Jiménez-Serra et al. 2021) and TMC-1 (Gratier et al. 2016; Cabezas et al. 2021; Agúndez et al. 2025) as representative of low-mass prestellar cores (LMPCs), I00117-MM2 and G11.11 as typical high-mass prestellar core candidates and/or IRDC environment (Vasyunina et al. 2014; Fontani et al. 2015; Mininni et al. 2021), IRAS 16293B and G31.41+0.31 represent typical corinos and hot cores, respectively (Kolesniková et al. 2014; Brinkmann et al. 2020; Feng et al. 2015; Mininni et al. 2023; López-Gallifa et al. 2024; Gorai et al. 2024). Finally, we have considered the comets 67P/Churyumov–Gerasimenko and Hale–Bopp (Bockelée-Morvan et al. 2000; Le Roy et al. 2015; Altwegg et al. 2016). The comparison is presented in Figure 4 where COMs abundances have been reported with respect to methanol.

From Figure 4, all COM abundances normalised to methanol are consistent with the typical cometary environment, similarly to the D-bearing species analysed in this work. The CH<sub>3</sub>CCH abundance normalised to methanol is significantly lower than that observed in typical dark sources but higher than or at most similar to that expected in warmer sources. CH<sub>3</sub>CCH is known to be a reliable tracer of gas excitation conditions (e.g. Taniguchi et al. 2018; Calcutt et al. 2019). Although its formation pathways are highly uncertain, this species has been detected in a plethora of environments, including external galaxies (Mauersberger et al. 1991; Qiu et al. 2020). While CH<sub>3</sub>CCH is often regarded as a tracer of intermediate temperatures in

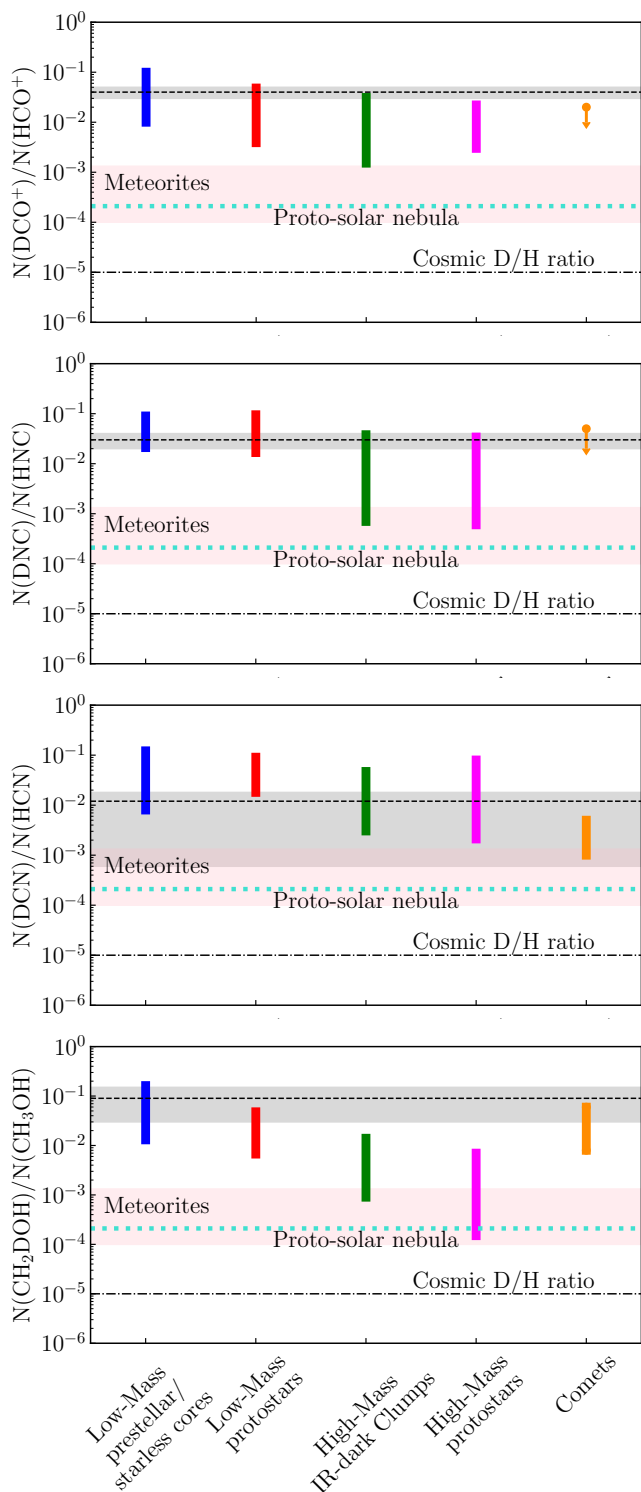


**Fig. 3.** D/H ratios measured from  $\text{DCO}^+$ ,  $\text{DNC}$ ,  $\text{DCN}$  and  $\text{CH}_2\text{DOH}$  toward the Clump (dashed black lines and grey shadows) compared with literature values across low-mass starless/pre-stellar cores and low-mass protostars, high-mass IR-dark clump, high-mass protostellar objects and comets. For reference, the cosmic D/H ratio (dotted-dashed black line; Oliveira et al. 2003) and the D/H measured in meteorites (red shadow) and proto-solar nebula (dotted cyan line) are reported.

high-mass star forming cores (Fontani et al. 2002), it can be found also in hot cores and hot corinos, both associated with the cold envelope ( $T < 60$  K) and a hotter, inner, component ( $T > 100$  K; Herbst & van Dishoeck 2009). Toward the Clump,

we report very low  $T_{\text{ex}} \sim 7$  K. At these low values of excitation temperature, the kinetic temperature is expected to be similar (Walmsley & Ungerechts 1983; Zeng et al. 2018), indicating that the  $\text{CH}_3\text{CCH}$  emission is associated with cold gas, i.e., not compatible with hot core/corinos conditions as seen in Figure 4. This is also supported by the lack of IR point-like source within the beam. However, from Figure 4, the  $\text{CH}_3\text{CCH}$  abundance with respect to  $\text{CH}_3\text{OH}$  is also slightly lower than what was reported toward L1544 and TMC-1. A possible explanation is that the emission from these species is unresolved in our single pointing data and may have different spatial extent. This is instead not the case for L1544 and TMC-1 which are closer and have been studied in much more detail, leading to more accurate measurements. Moreover, while the Clump is not spatially coincident with the shock front detected in Cosentino et al. (2018, 2019), it is possible that some contamination is present within the beam. Higher-angular resolution images will shed light on these scenarios.

Contrary to  $\text{CH}_3\text{CCH}$ , the species  $\text{CH}_3\text{CHO}$  shows abundance with respect to methanol consistent with that of typical LMPSCs and slightly higher than that observed in warmer regions. Indeed, the low excitation temperature measured for this species,  $T_{\text{ex}} \sim 5$  K, suggests that the emission may be sub-thermally excited. Moreover, the ratio with respect to  $\text{CH}_3\text{OH}$  reported here,  $\sim 0.03$ , is more than one order of magnitude larger than that typically measured in shocks from molecular outflows ( $10^{-4}$ - $10^{-3}$ ; Holdship et al. 2019; Codella et al. 2020; López-Sepulcre et al. 2024).

$\text{CH}_3\text{CN}$ , as seen in Figure 4, shows an abundance with respect to methanol significantly lower than that measured in LMPSCs (e.g. Bhat et al. 2023) and consistent with that typically measured in hot corinos but not towards hot cores. Similarly to  $\text{CH}_3\text{CCH}$ , this may be due to the fact that the true emission spatial extent remains unresolved in our observations leading to beam-dilution effects at the larger source distance.  $\text{CH}_3\text{CN}$  has been widely used to investigate the physical conditions of warm environments, and Codella et al. (2009) showed that it can be efficiently produced also in shocked regions. While the excitation temperature measured here is lower than that reported by Codella et al. (2009), the abundance with respect to methanol is consistent with that reported toward the shocked knots of the L1157 outflows (see also Arce et al. 2008).

From Figure 4, the  $\text{CH}_3\text{SH}$  abundance w.r.t. methanol is consistent with that estimated toward low-mass starless/prestellar cores and hot cores. Toward LMPSCs, it has been suggested that  $\text{CH}_3\text{SH}$  forms onto the icy mantle of dust grains and it is then released into the gas phase through non-thermal processes, such as cosmic ray-induced desorption (e.g. Zhou et al. 2022). However, the formation pathway of these species is still unclear and follow-up high-resolution observations are needed to spatially resolve the emission and further constrain the emitting regions for  $\text{CH}_3\text{SH}$  and  $\text{CH}_3\text{CN}$ .

## 5. Summary and Conclusions

We have presented high-sensitivity single pointing observations obtained at 3 mm (IRAM 30m) and 7 mm (Yebes 40m) toward the shock-induced potentially prestellar cluster known as the Clump (Cosentino et al. 2023). Within the large bandwidth spectra, we have identified multiple D-bearing species such as  $\text{DCO}^+$ ,  $\text{DNC}$ ,  $\text{DCN}$  and  $\text{CH}_2\text{DOH}$  as well as multiple COMs, i.e.,  $\text{CH}_3\text{OH}$ ,  $\text{CH}_3\text{CHO}$ ,  $\text{CH}_3\text{CCH}$ ,  $\text{CH}_3\text{CN}$  and  $\text{CH}_3\text{SH}$ . The D/H ratios measured from the detected D-bearing species and their H-bearing counterparts are several order of magnitude

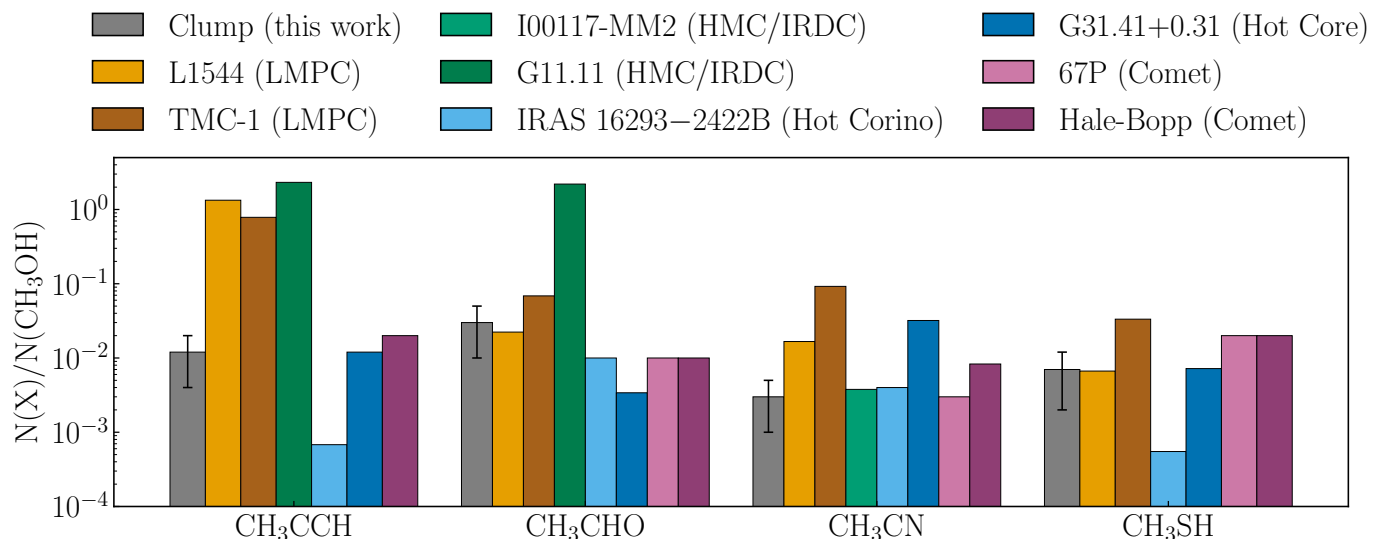


**Fig. 4.** Comparison between COM abundances with respect to CH<sub>3</sub>OH measured toward the Clump and literature values toward L1544 (LMPC; Vastel et al. 2014; Bizzocchi et al. 2014; Jiménez-Serra et al. 2016; Vastel et al. 2019), TMC-1 (dark clouds Gratier et al. 2016; Cabezas et al. 2021; Agúndez et al. 2025), I00117-MM2 and G11.11 (high-mass cores and/or IRDCs Vasyunina et al. 2014; Fontani et al. 2015; Mininni et al. 2021), IRAS 16293B (hot corino) and G32.41+0.31 (hot core; Mininni et al. 2023; López-Gallifa et al. 2024), and the comets 67P/Churyumov–Gerasimenko and Hale–Bopp (Bockelée-Morvan et al. 2000; Le Roy et al. 2015; Altwegg et al. 2016). Colors are representative of the environment: orange and dark orange for low-mass cores and dark clouds, green and dark green for massive cores/IRDCs, blue and dark blue for more evolved hot cores and corinos, pink and purple for comets.

larger than the typical cosmic D/H ratio and broadly consistent with those observed in low-mass starless/pre-stellar cores. Within the high-sensitivity spectra, we also detected multiple COMs. The Clump shows a level of chemical complexity similar to that reported toward some young low-mass prestellar cores (younger than L1544) such as L1517B (Megías et al. 2023). This may be indicative of the source evolutionary stage, as already reported toward other low-mass starless cores. Alternatively, this may be a consequence of beam dilution effects. Among the detected species, CH<sub>3</sub>CHO and CH<sub>3</sub>SH show abundance w.r.t. methanol consistent with that observed in low-mass starless/pre-stellar cores. On the other hand, the CH<sub>3</sub>CCH and CH<sub>3</sub>CN abundance normalised to methanol is slightly lower than values reported in low-mass environments, suggesting potential contamination from shocked gas. The chemical complexity and Deuterium content of the region are consistent with the shock timescales estimated in Cosentino et al. (2019). Indeed, the enhanced densities reported for the post-shocked gas shorten the CO depletion time-scale, boosting the production of deuterated species (Lis et al. 2002, 2016). For the post-shock density estimated by Cosentino et al. (2019), the CO depletion timescale is expected to be  $\leq 10^4$  yrs (Caselli et al. 1999), consistent with both the shock dynamical age (few  $10^4$  yr; Cosentino et al. 2019) and the SNR age (20 kyr). Finally, we have compared the abundances of all detected D-bearing species and COMs with those observed in comets and found a broad agreement. This similarity suggests that COM and Deuterium budgets could be inherited from the compressed, cold and dense post-shocked material, where the shock passage has enabled a fast chemistry. In light of all this, we suggest that the Clump is a shock-induced dense core at the very early stage of evolution with the potential to undergo gravitational collapse and form the next generation of protostars in the cloud. We also speculate that stellar-feedback slow-shocks may contribute to set the initial chemical conditions of star formation, which is later on inherited by comets. Follow-up high-angular resolution images are needed to remove potential beam

dilution effect and separate the emission arising from cores and the shocked gas. Nevertheless, at the best of our knowledge, this represents the first detection of COMs toward a SNR-molecular cloud interaction site, and it is a potentially unique signature of chemically enriched, post-shock dense core formation. Finally, shocks from late-stage SNRs are intrinsically gentler and more spatially extended than those observed in molecular outflows. Hence, if some of the detected COMs have been released into the gas phase by the SNR-shock passage, this may lead the way to new investigation into COMs survival in shocked environments.

*Acknowledgements.* This work is based on observations carried out under project number 027-21 with the IRAM 30 m telescope. IRAM is supported by INSU/CNRS (France), MPG (Germany) and IGN (Spain). This work is also based on observations carried out with the Yebes 40m telescope (project 24A019). The 40m radio telescope at Yebes Observatory is operated by the Spanish Geographic Institute (IGN; Ministerio de Transportes, Movilidad y Agenda Urbana). J.C.T. acknowledges support from ERC project 788829–MSTAR. I.J.-S. acknowledges funding from grant PID2022-136814NB-I00 funded by the Spanish Ministry of Science, Innovation and Universities/State Agency of Research MICIU/AEI/ 10.13039/501100011033 and by “ERDF/EU”. R.F. acknowledges support from the grants Juan de la Cierva FJC2021-046802-I, PID2020-114461GB-I00 and CEX2021-001131-S funded by MCIN/AEI/ 10.13039/501100011033 and by “European Union NextGenerationEU/PRTR”. S.V. acknowledges partial funding from the European Research Council (ERC) Advanced Grant MOPPEX 833460.

## References

- Adams, F. C. 2010, *Annual Review of Astronomy and Astrophysics*, 48, 47  
 Agertz, O., Kravtsov, A. V., Leitner, S. N., & Gnedin, N. Y. 2013, *ApJ*, 770, 25  
 Agúndez, M., Cernicharo, J., & Guélin, M. 2015, *A&A*, 577, L5  
 Agúndez, M., Molpeceres, G., Cabezas, C., et al. 2025, *A&A*, 693, L20  
 Alexander, C. M. O., Bowden, R., Fogel, M. L., et al. 2012, *Science*, 337, 721  
 Alexander, C. M. O., Fogel, M. L., Yabuta, H., & Cody, G. D. 2007, *Geochimica et Cosmochimica Acta*, 71, 4380  
 Alexander, C. M. O., McKeegan, K. D., & Altwegg, K. 2017, *Space Science Reviews*, 212, 1151  
 Alexander, C. M. O., Newsome, S. D., Fogel, M. L., et al. 2010, *Geochimica et Cosmochimica Acta*, 74, 4417

- Altwegg, K., Balsiger, H., Bar-Nun, A., et al. 2016, *Science Advances*, 2, e1600285
- Ambrose, H. et al. 2024, *Journal name, update with correct bib info*
- Appel, S. M., Burkhart, B., Semenov, V. A., et al. 2023, *ApJ*, 954, 93
- Arce, H. G., Santiago-García, J., Jørgensen, J. K., Tafalla, M., & Bachiller, R. 2008, *ApJ*, 681, L21
- Arzoumanian, D., Arakawa, S., Kobayashi, M. I. N., et al. 2023, *ApJ*, 947, L29
- Bally, J. 2011, in *Computational Star Formation*, ed. J. Alves, B. G. Elmegreen, J. M. Girart, & V. Trimble, Vol. 270, 247–254
- Barnes, A. T., Henshaw, J. D., Fontani, F., et al. 2021, *MNRAS*, 503, 4601
- Barnes, A. T., Kong, S., Tan, J. C., et al. 2016, *MNRAS*, 458, 1990
- Barnes, A. T., Liu, J., Zhang, Q., et al. 2023, *A&A*, 675, A53
- Beattie, J. R., Noer Kolborg, A., Ramirez-Ruiz, E., & Federrath, C. 2025, *arXiv e-prints*, arXiv:2501.09855
- Beuther, H., Bihr, S., Rugel, M., et al. 2016, *A&A*, 595, A32
- Bhat, B., Kar, R., Mondal, S. K., et al. 2023, *ApJ*, 958, 111
- Bianchi, E., Codella, C., Ceccarelli, C., et al. 2017, *MNRAS*, 467, 3011
- Bianchi, E., Codella, C., Ceccarelli, C., et al. 2019, *MNRAS*, 483, 1850
- Biver, N., Bockelée-Morvan, D., Paubert, G., et al. 2019, *Astronomy & Astrophysics*, 630, A19
- Bizzocchi, L. et al. 2014, *Astronomy & Astrophysics*, methanol maps in starless cores :contentReference[oaicite:2]index=2
- Blake, G. A., Sutton, E. C., Masson, C. R., & Phillips, T. G. 1987, *ApJ*, 315, 621
- Bockelée-Morvan, D., Lis, D. C., Wink, J. E., et al. 2000, *Astronomy & Astrophysics*, 353, 1101
- Boss, A. P. & Keiser, S. A. 2010, *The Astrophysical Journal Letters*, 717, L1–L5
- Boss, A. P. & Keiser, S. A. 2013, *The Astrophysical Journal*, 776, 72
- Boucasse, L. et al. 2022, *Journal name, update with correct bib info*
- Bovino, S., Lupi, A., Giannetti, A., et al. 2021, *A&A*, 654, A34
- Brinkmann, N., Wyrowski, F., Kauffmann, J., et al. 2020, *A&A*, 636, A39
- Brown, R. D., Crofts, J. G., Gardner, F. F., et al. 1975, *ApJ*, 197, L29
- Busemann, H., Young, A. F., Alexander, C. M. O., et al. 2006, *Science*, 312, 727
- Butler, M. J. & Tan, J. C. 2009, *ApJ*, 696, 484
- Butler, M. J. & Tan, J. C. 2012, *ApJ*, 754, 5
- Cabezas, C., Agúndez, M., Marcelino, N., et al. 2021, *A&A*, 654, L9
- Calcutt, H., Willis, E. R., Jørgensen, J. K., et al. 2019, *A&A*, 631, A137
- Carey, S. J., Noriega-Crespo, A., Mizuno, D. R., et al. 2009, *PASP*, 121, 76
- Caselli, P., Vastel, C., Ceccarelli, C., et al. 2008, *A&A*, 492, 703
- Caselli, P., Walmsley, C. M., Tafalla, M., Dore, L., & Myers, P. C. 1999, *ApJ*, 523, L165
- Cazaux, S., Tielens, A. G. G. M., Ceccarelli, C., et al. 2003, *ApJ*, 593, L51
- Ceccarelli, C., Caselli, P., Bockelée-Morvan, D., et al. 2014, *Protostars and Planets VI*, 859
- Ceccarelli, C., Codella, C., Balucani, N., et al. 2022, *arXiv e-prints*, arXiv:2206.13270
- Cernicharo, J., Agúndez, M., Cabezas, C., et al. 2021, *A&A*, 649, L15
- Cheng, Y., Tan, J. C., Caselli, P., et al. 2021, *ApJ*, 916, 78
- Churchwell, E., Babler, B. L., Meade, M. R., et al. 2009, *PASP*, 121, 213
- Codella, C., Benedettini, M., Beltrán, M. T., et al. 2009, *A&A*, 507, L25
- Codella, C., Ceccarelli, C., Bianchi, E., et al. 2020, *A&A*, 635, A17
- Coletta, A., Fontani, F., Rivilla, V. M., et al. 2020, *A&A*, 641, A54
- Colzi, L., Martín-Pintado, J., Rivilla, V. M., et al. 2022, *ApJ*, 926, L22
- Cosentino, G., Jiménez-Serra, I., Barnes, A. T., et al. 2025, *A&A*, 693, A199
- Cosentino, G., Jiménez-Serra, I., Caselli, P., et al. 2019, *ApJ*, 881, L42
- Cosentino, G., Jiménez-Serra, I., Henshaw, J. D., et al. 2018, *MNRAS*, 474, 3760
- Cosentino, G., Jiménez-Serra, I., Tan, J. C., et al. 2022, *MNRAS*, 511, 953
- Cosentino, G., Tan, J. C., Jiménez-Serra, I., et al. 2023, *A&A*, 675, A190
- Crapsi, A., Caselli, P., Walmsley, C. M., et al. 2005, *ApJ*, 619, 379
- Crovisier, J., Bockelée-Morvan, D., Colom, P., Biver, N., & Bockelée-Morvan, D. 2004, *Comets II*, 273
- Desch, S. J., Young, E. D., Dunham, E. T., Fujimoto, Y., & Dunlap, D. R. 2022, *Protostars and Planets VII*, 759
- Despois, D., Bockelée-Morvan, D., Crovisier, J., & Biver, N. 2005, *Bulletin of the American Astronomical Society*, 37, 647
- Drozdovskaya, M. N., Schroeder, I. R. H. G., Rubin, M., et al. 2021, *Monthly Notices of the Royal Astronomical Society*, 500, 4901, arXiv:2010.12489
- Emprechtinger, M., Caselli, P., Volgenau, N. H., Stutzki, J., & Wiedner, M. C. 2009, *A&A*, 493, 89
- Endres, C. P., Schlemmer, S., Schilke, P., Stutzki, J., & Müller, H. S. P. 2016, *Journal of Molecular Spectroscopy*, 327, 95
- Federrath, C. & Klessen, R. S. 2012, *ApJ*, 761, 156
- Feng, S., Beuther, H., Henning, T., et al. 2015, *A&A*, 581, A71
- Fontani, F., Busquet, G., Palau, A., et al. 2015, *A&A*, 575, A87
- Fontani, F., Caselli, P., Crapsi, A., et al. 2006, *A&A*, 460, 709
- Fontani, F., Cesaroni, R., Caselli, P., & Olmi, L. 2002, *A&A*, 389, 603
- Fontani, F., Palau, A., Caselli, P., et al. 2011, *A&A*, 529, L7
- Fontani, F., Sakai, T., Furuya, K., et al. 2014, *MNRAS*, 440, 448
- Fragile, P. C., Murray, S. D., & Lin, D. N. C. 2003, *The Astrophysical Journal*, 590, 778
- Friesen, R. K., Kirk, H. M., & Shirley, Y. L. 2013, *ApJ*, 765, 59
- Gerner, T., Shirley, Y. L., Beuther, H., et al. 2015, *A&A*, 579, A80
- Gorai, P., Law, C.-Y., Tan, J. C., et al. 2024, *ApJ*, 960, 127
- Gounelle, M. & Meynet, G. 2012, *Astronomy & Astrophysics*, 545, A4
- Gratier, P. et al. 2016, *Astronomy & Astrophysics*, see Gratier et al. analysis compared in Taquet et al. 2017 :contentReference[oaicite:1]index=1
- Herbst, E. & van Dishoeck, E. F. 2009, *ARA&A*, 47, 427
- Hernandez, A. K. & Tan, J. C. 2015, *ApJ*, 809, 154
- Hirota, T., Ikeda, M., & Yamamoto, S. 2001, *Astrophysical Journal*, 547, 814
- Hogge, T. G., Jackson, J. M., Allingham, D., et al. 2019, *ApJ*, 887, 79
- Holdship, J., Viti, S., Codella, C., et al. 2019, *ApJ*, 880, 138
- Imai, M., Furuya, K., & Aikawa, Y. 2018, *Astrophysical Journal*, 869, 34
- Inoue, T., Hennebelle, P., Fukui, Y., et al. 2018, *PASJ*, 70, S53
- Jiménez-Serra, I., Vasyunin, A. I., Caselli, P., et al. 2016, *ApJ*, 830, L6
- Jiménez-Serra, I., Vasyunin, A. I., Spezzano, S., et al. 2021, *ApJ*, 917, 44
- Jørgensen, J. K., Hogerheijde, M. R., Blake, G. A., et al. 2004, *A&A*, 415, 1021
- Kai, A. et al. 2024, *Journal name, update with correct bib info*
- Kainulainen, J. & Tan, J. C. 2013, *A&A*, 549, A53
- Khullar, S., Matzner, C. D., Murray, N., et al. 2024, *ApJ*, 973, 40
- Kolesníková, L., Tercero, B., Cernicharo, J., et al. 2014, *ApJ*, 784, L7
- Kong, S., Tan, J. C., Caselli, P., et al. 2016, *ApJ*, 821, 94
- Le Roy, L., Altwegg, K., Balsiger, H., et al. 2015, *Astronomy & Astrophysics*, 583, A1
- Lee, Y.-H., Koo, B.-C., & Lee, J.-J. 2020, *AJ*, 160, 263
- Leitherer, C., Schaerer, D., Goldader, J. D., et al. 1999, *ApJS*, 123, 3
- Lellouch, E., Bézard, B., Fouchet, T., et al. 2001, *A&A*, 370, 610
- Li, S., Frank, A., Blackman, E. G., et al. 2014, *The Astrophysical Journal*, 789, 10
- Lis, D. C., Gerin, M., Phillips, T. G., & Motte, F. 2002, *ApJ*, 569, 322
- Lis, D. C., Wootten, H. A., Gerin, M., et al. 2016, *ApJ*, 827, 133
- López-Gallifa, Á., Rivilla, V. M., Beltrán, M. T., et al. 2024, *MNRAS*, 529, 3244
- López-Sepulcre, A., Codella, C., Ceccarelli, C., Podio, L., & Robuschi, J. 2024, *A&A*, 692, A120
- Manigand, S., Calcutt, H., Jørgensen, J. K., et al. 2019, *A&A*, 623, A69
- Marcelino, N., Agúndez, M., Tercero, B., et al. 2020, *A&A*, 643, L6
- Martín, S., Martín-Pintado, J., Blanco-Sánchez, C., et al. 2019, *A&A*, 631, A159
- Martín-Doménech, R., Bergner, J. B., Öberg, K. I., et al. 2021, *ApJ*, 923, 155
- Mauersberger, R., Henkel, C., Walmsley, C. M., Sage, L. J., & Wiklind, T. 1991, *A&A*, 247, 307
- Megías, A., Jiménez-Serra, I., Martín-Pintado, J., et al. 2023, *MNRAS*, 519, 1601
- Meier, R., Owen, T. C., Matthews, H. E., et al. 1998, *Science*, 279, 1707
- Mininni, C., Beltrán, M. T., Colzi, L., et al. 2023, *A&A*, 677, A15
- Mininni, C., Fontani, F., Sánchez-Monge, A., et al. 2021, *A&A*, 653, A87
- Molinari, S., Swinyard, B., Bally, J., et al. 2010, *PASP*, 122, 314
- Öberg, K. I., Loomis, C. J., et al. 2023, *arXiv preprint*, arXiv:2212.14529v3
- Oliveira, C. M., Hébrard, G., Howk, J. C., et al. 2003, *ApJ*, 587, 235
- Ouellette, N., Desch, S. J., & Hester, J. J. 2007, *The Astrophysical Journal*, 662, 1268
- Ouellette, N., Desch, S. J., & Hester, J. J. 2009, *Geochimica et Cosmochimica Acta*, 73, 4946
- Parise, B., Castets, A., Herbst, E., et al. 2004, *A&A*, 416, 159
- Parker, R. J., Lichtenberg, T., Patel, M., Polius, C. K. M., & Riddill-Smith, M. 2023, *MNRAS*, 521, 4838
- Paron, S., Ortega, M. E., Rubio, M., & Dubner, G. 2009, *A&A*, 498, 445
- Petrashkevich, L., Sipilä, O., et al. 2024, *Journal name, update with correct bib info*
- Pfalzner, S., Davies, M., Gounelle, M., et al. 2015, *Physica Scripta*, 90, 068001
- Pickett, H. M., Poynter, R. L., Cohen, E. A., et al. 1998, *J. Quant. Spectr. Rad. Transf.*, 60, 883
- Qiu, J., Zhang, J., Zhang, Y., Jia, L., & Tang, X. 2020, *A&A*, 634, A125
- Rathborne, J. M., Jackson, J. M., & Simon, R. 2006, *ApJ*, 641, 389
- Reach, W. T., Tram, L. N., DeWitt, C., et al. 2024, *ApJ*, 977, 149
- Redaelli, E., Bizzocchi, L., Caselli, P., et al. 2019, *Astronomy & Astrophysics*, 629, A15
- Remusat, L., Robert, F., Meibom, A., Binet, L., & Gourier, D. 2006, *Proceedings of the National Academy of Sciences*, 103, 17462
- Robert, F. 2003, *Space Science Reviews*, 106, 87
- Romero-Mirza, C. E., Öberg, K. I., Law, C. J., et al. 2022, *arXiv preprint*, arXiv:2212.06912
- Sabatini, G., Giannetti, A., Bovino, S., et al. 2019, *MNRAS*, 490, 4489
- Sano, H., Inoue, T., Tokuda, K., et al. 2020, *ApJ*, 904, L24
- Sano, H., Yamane, Y., van Loon, J. T., et al. 2023, *ApJ*, 958, 53
- Sashida, T., Oka, T., Tanaka, K., et al. 2013, *ApJ*, 774, 10
- Scibelli, S., Shirley, Y., Megías, A., & Jiménez-Serra, I. 2024, *MNRAS*, 533, 4104
- Scibelli, S., Shirley, Y., Vasyunin, A., & Launhardt, R. 2021, *MNRAS*, 504, 5754
- Skrutskie, M. F., Cutri, R. M., Stiening, R., et al. 2006, *AJ*, 131, 1163
- Taniguchi, K., Saito, M., Majumdar, L., et al. 2018, *ApJ*, 866, 150
- Thiel, V., Belloche, A., Menten, K. M., Garrod, R. T., & Müller, H. S. P. 2017, *A&A*, 605, L6

- van Gelder, M. L., Tabone, B., Hogerheijde, M. R., et al. 2021, *Astronomy & Astrophysics*, 653, A159
- van Gelder, M. L., Tabone, B., Hogerheijde, M. R., et al. 2022, *Astronomy & Astrophysics*, 659, A186
- Vastel, C., Ceccarelli, C., Lefloch, B., & Bachiller, R. 2014, arXiv e-prints, arXiv:1409.6565
- Vastel, C., Loison, J. C., Wakelam, V., & Lefloch, B. 2019, *A&A*, 625, A91
- Vasyunina, T., Vasyunin, A. I., Herbst, E., et al. 2014, *ApJ*, 780, 85
- Walmsley, C. M. & Ungerechts, H. 1983, *A&A*, 122, 164
- Walsh, C., Millar, T. J., Nomura, H., et al. 2014, *A&A*, 563, A33
- Young, E. D. 2014, *Earth and Planetary Science Letters*, 392, 16
- Zeng, S., Jiménez-Serra, I., Cosentino, G., et al. 2017, *A&A*, 603, A22
- Zeng, S., Jiménez-Serra, I., Rivilla, V. M., et al. 2018, *MNRAS*, 478, 2962
- Zhou, C., Vastel, C., Montillaud, J., et al. 2022, *A&A*, 658, A131
- Zhou, Y., Xu, J.-L., Li, D., Li, H.-B., & Wang, J.-J. 2021, *Astronomy & Astrophysics*, 654, A19

## Appendix A: Spectra of detected species

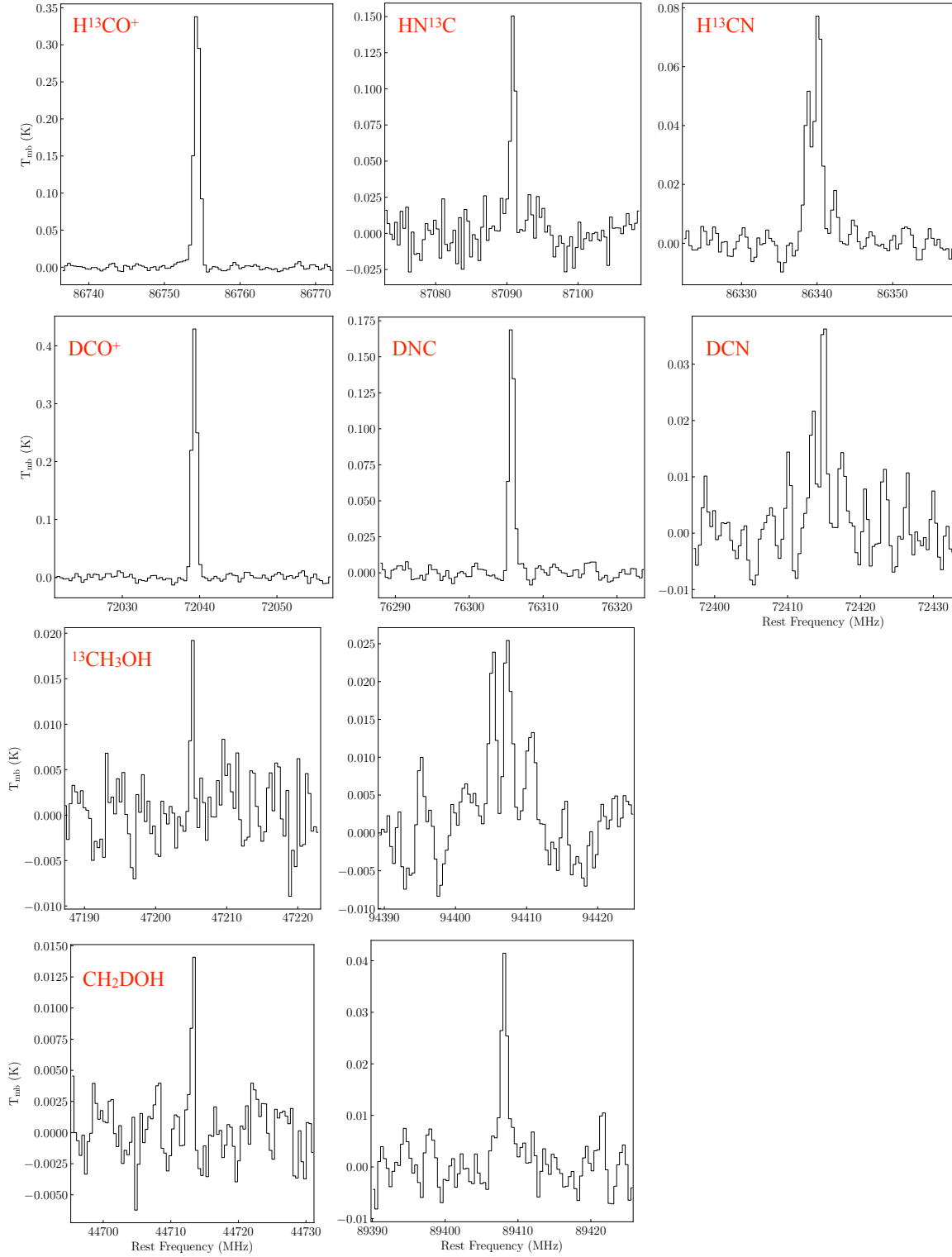


**Fig. A.1.** Spectra of detected D-bearing species and their H-bearing counterparts. For clarity, we only indicate the species, while quantum numbers for each transition are reported in Table 2.

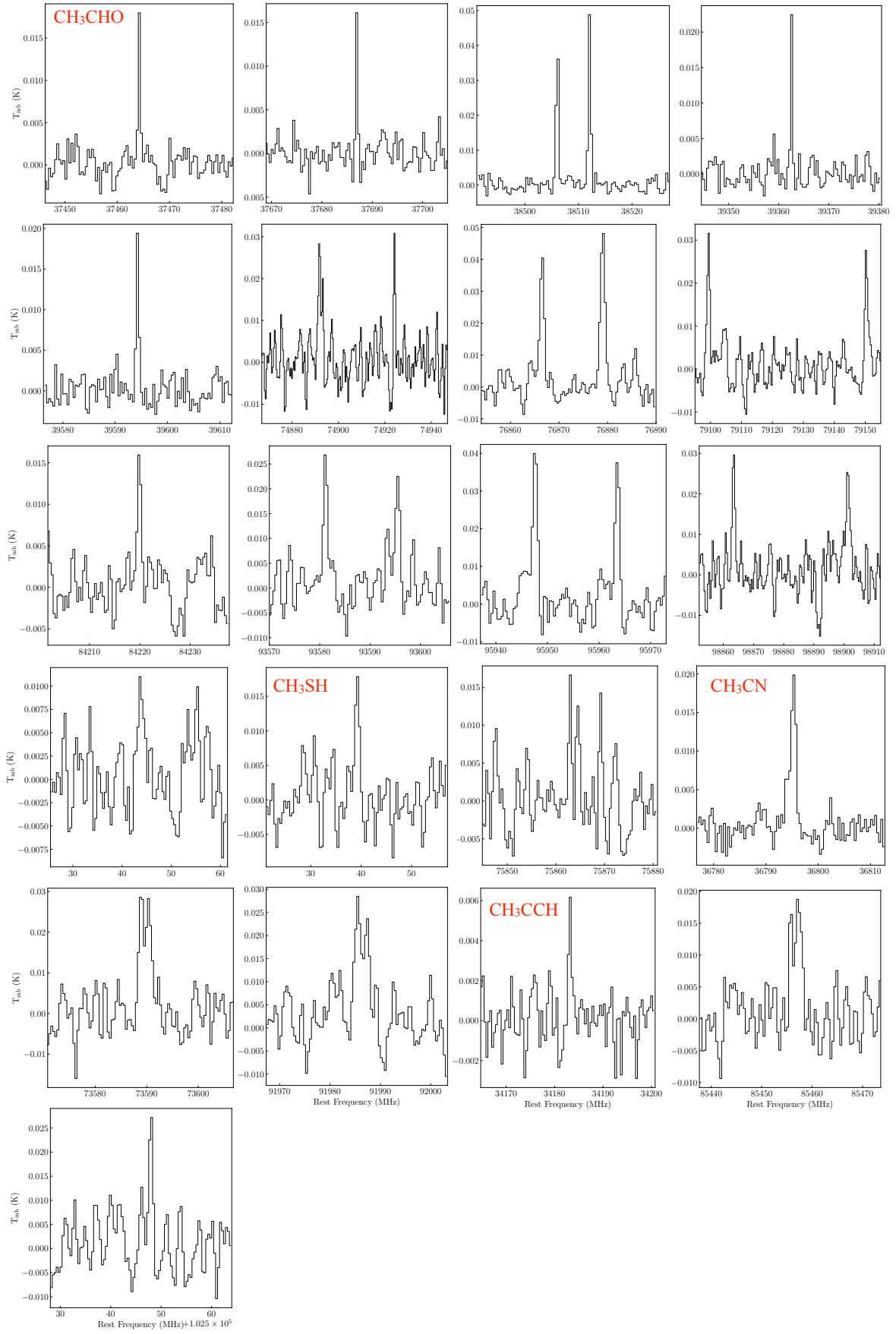


**Fig. A.2.** Spectra of detected COMs. For clarity, we only indicate the species, while quantum numbers for each transitions are reported in Table 2.